Noname manuscript No.
(will be inserted by the editor)

An experimental study of the rotational effects on separated turbulent flow during stall delay

Yanhua Wu · Hsiao Mun Lee · Hui Tang · Martin Skote · Yong Shan

Received: date / Accepted: date

Abstract Three-dimensional velocity fields were measured using tomographic particle image velocimetry (Tomo-PIV) on a model of the blade of a small-scale horizontal axis wind turbine (HAWT) to study the effects of rotation on separated turbulent flows during stall delay at a global tip speed ratio (TSR) of 3 and a Reynolds number of 4800. The flow fields on a static airfoil were also measured at a similar angle-of-attack (AOA) and Reynolds number for comparison. It was observed that the blade's rotation in the streamwise direction significantly affected both the mean flow and the turbulence statistics over the suction surface. The mean velocity fields revealed that, different from the airfoil flow at large AOA, the recirculation region with reversed flow did not exist on the suction surface of the blade and the flow was rather attached. Mean spanwise flow from blade's root to its tip was also generated by the rotation. The mean vorticity vector of the blade flow was found to be tilted in the rotational direction of the blade, as well as in the wall-normal direction. Of particular effects of the rotation on Reynolds stresses were the enhancement of $\langle w^2 \rangle$ and the creation of strong $\langle vw \rangle$. The production of Reynolds stresses was also affected by blade's rotation directly through

Y. Wu
School of Mechanical and Aerospace Engineering
Nanyang Technological University, Singapore
E-mail: yanhuawu@ntu.edu.sg

H.M. Lee
School of Mechanical and Aerospace Engineering
Nanyang Technological University, Singapore
Present address: National University of Singapore

H. Tang
Department of Mechanical Engineering
The Hong Kong Polytechnic University, Hung Hom, Kowloon, Hong Kong

M. Skote
School of Mechanical and Aerospace Engineering
Nanyang Technological University, Singapore

Y. Shan
College of Energy & Power Engineering
Nanjing University of Aeronautics & Astronautics, China

the rotational production terms and indirectly by dramatically changing the fluctuating velocity fields. The distribution of enstrophy was observed to be modified by rotation, too.

Keywords rotational effects · separated turbulent flow · stall delay · horizontal axis wind turbine · Tomographic PIV

1 Introduction

The use of two-dimensional steady-state airfoil data in the actuator disc theory results in unsatisfactory predictions of wind turbine loads when operating in yaw and at high wind speeds. One of the well-known differences is that the angle of attack (AOA) at which stall occurs for a rotating wind turbine blade was found to be larger than that for a static airfoil, a phenomenon called stall delay. The science behind this engineering phenomenon has been studied in the past in a limited number of works [1–11]. The main discoveries from these research included reduced size of the flow separation, stabilization of the shedding vortices, existence of the spanwise flow, and the reduction of the adverse pressure gradients due to Coriolis force and/or external pressure modifications. However, much more work needs to be done in order to significantly improve our primitive understanding of the fluid physics of stall delay.

In particular, in the experimental studies of Lee and Wu [9–11], the existence of turbulent flows was observed at the inboard (close to the blade's root) section of the turbine blade when the incoming flow was separated from the blade's leading edge. Therefore, it is expected that the turbulence inside the separated flow on the suction surface is also going to be affected by the rotation of the blade. The objective of this paper is to investigate those effects of rotation on the characteristics of the separated turbulent flows during stall delay by comparing to the static airfoil case.

In the literature, most of the past studies on the effects of rotation on turbulence for flows relevant to turbomachinery were performed with a spanwise rotation [12–17], which means that the rotation vector is parallel to the mean flow vorticity. These research are more relevant to the radial flows rather than the axial flow of the wind turbine studied herein. Although a majority of them were dealing with rotating channel flows, a few [18, 19] have investigated the spanwise rotated backward-facing-step turbulence in which a massive flow separation occurred, similar to what happens at the inboard section of the turbine blade during stall delay. The studies on the effects of rotation on turbomachiery related flows with a streamwise rotational component started to appear in the last decade, but mainly from two research groups [20–22] and only on turbulent channel flows. Since it appears that no research has ever been done so far on how the streamwise rotation affects the separated turbulent flow, as in the case of the current study, the following literature review will summarize the current state-of-the-art on the spanwise rotation of backward-facing-step flows and streamwise rotation of the channel flows separately.

Barri and Andersson [18] applied direct numerical simulations on a turbulent backward-facing step flow subject to spanwise rotations. They found that the separation bubbles with recirculation flow became smaller with increasing rotational rates, which is due to the increase of the cross-stream (wall-normal and spanwise directions) turbulence intensity in the anti-cyclonic shear layer formed between the bulk flow and the recirculation bubble. Significantly high levels of velocity fluctuations were also observed in the spanwise direction close to the reattachment behind the step, thanks to the longitudinal Taylor-Gortler-like roll cells extending into the backflow. Measurements of velocity fields were performed by Visscher and Andersson [19] using particle image velocimetry on the separated flow downstream of a backward-facing step in a spanwise rotating channel. The experments were made with 13 different rotation numbers at a bulk Reynolds number of 5600. The mean flow patterns were observed to be dramatically affected by the system rotation. Specifically, the recirculation region was decreased with larger anti-cyclonic rotation while it was increased by the cyclonic rotation. The Reynolds normal and shear stresses were also observed to be severely affected by the spanwise rotation. The anti-cyclonic rotation enhanced the turbulence level in the mixing layer resulting in a higher spreading rate, while the cyclonic rotation exerted the reverse effects.

The effects of arbitrary system rotation on the turbulent channel flows were studied by Wu and Kasagi [20] using a series of direct numerical simulations. They observed that the streamwise rotation, if stronger than the spanwise rotation, could enhance not only the turbulence on the suction side but also the secondary flow which rotated in the positive streamwise direction. Recktenwald et al. [21] studied the streamwise rotated turbulent channel flow using both direct numerical simulation and particle image velocimetry measurements. It was found that the streamwise rotation mainly affected the components of the Reynolds shear stresses involving the spanwise velocity component. Through the two-point velocity correlation coefficients, the length scales of the flow structures were also observed increased in all three directions. A large-eddy simulation of streamwise-rotating turbulent channel flow was performed by Alkishriwi et al. [22] at Re_τ=180. The results showed the development of a secondary flow in the spanwise direction, which became stronger with higher rotational speed. In addition, they observed a distortion of the mean velocity profile, the slight decrease of the streamwise Reynolds stress close to the walls, and a significant increase of the spanwise Reynolds stress not only near the walls but also in the center of the channel.

2 Experiments

Details of the experiments were reported in Lee and Wu [9–11] and only a brief summary is provided here. Measurements were conducted in a wind tunnel with a test section of 0.4m×0.4m with a freestream turbulence intensity of about 0.4%. The rotating blade studied is a down-scaled model of the wind turbine blade designed using the blade element momentum (BEM) method for a 5 KW horizontal-axis wind turbine (HAWT). The design tip-speed-ratio, TSR=$\frac{\Omega R}{V_\infty}$, is 6, where Ω is the rotating speed of the blade, R is the radius of the blade which is 0.309m, and V_∞ is the freestream velocity. This single-blade rotor was oscillating about $\pm 25^\circ$ in the test section due to the limited size of the wind tunnel. The center of rotation is located at the center of the hub or shaft, as shown in Figure 1. Note that the separated turbulence on the current oscillating blade at the instant of time of the middle of the oscillation can be well representative of the turbulence

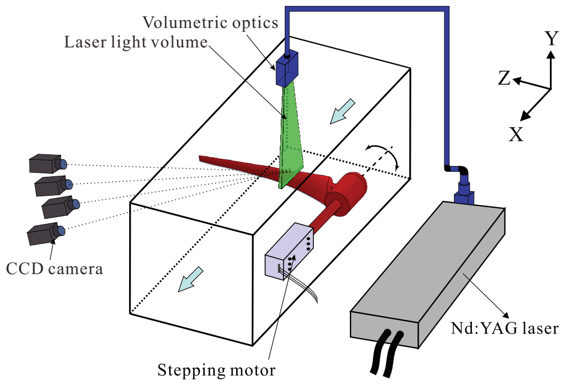

Fig. 1 Experimental setup of the Tomo-PIV measurements. In the current coordinate system, x is the freestream direction, z is along the span of the airfoil or the blade, and y is perpendicular to the other two directions and is perpendicular to the bottom wall of the wind tunnel's test section.

on the rotating blade that rotates with 360°. This is because the angle of attack and the relative velocity of the current oscillating blade are the same as those of a rotating blade, when our tomographic PIV measurements were performed at a time after the motor has already achieved a steady rotation. The similarity of the flow on the rotating blade to that on the oscillating blade at the middle of the oscillation has been substantiated by the similarities of the pressure distributions between a typical rotating blade during stall delay (Figure 3.74 in Ref.[23]) and the current setup (Figure 3 in Ref.[10]). Nevertheless, it is arguable that the transient effects due to the change of AOA in the oscillation might affect the second-order statistics presented below.

The experiments were performed at a TSR of 3 where stall delay was observed[10]. The angle of attack (AOA) on the blade at the center of the tomographic PIV measurement of $0.25R$ is approximately 30°. The Reynolds number Re=$V_r c/\nu$ is about 4800, where c is the chord length of the blade at the measurement location and V_r is the relative velocity which is determined by

$$V_r = \sqrt{V_\infty^2(1-a)^2 + (\Omega r)^2(1+a')^2}, \tag{1}$$

where r is the local radius of the blade, a is the axial induction factor and a' is the angular induction factor. Both a and a' were obtained from the BEM method during the design of the turbine blade. The AOA at each blade section can be estimated by [24] $AOA = \gamma - \beta$, where γ is the angle between the freestream velocity and chord. β is determined by $tan\beta = \frac{\lambda_r(1+a')}{(1-a)}$, where λ_r is the local TSR, and a & a' are axial and angular induction factors. A non-dimensional parameter to quantify the rotation is the upstream rotation number[18], $R_0 = \Omega c/V_\infty$, which is -0.34 in the current study. The negative sign of R_0 is due to the fact that the rotational vector $\mathbf{\Omega}$ is opposite to the positive x direction which is the direction of the incoming flow.

An S809 airfoil, the same airfoil shape used for the rotating blade, with the span of the wind tunnel's width and a chord of 0.03m was also fabricated in order to compare the turbulent flow on the suction surface of this static airfoil with that over the blade model. The Re and AOA for the measurements of the static airfoil were similar to those of the rotating blade. The blockage ratios for the blade and the airfoil are 5.5% and 3.8%, respectively.

Due to the intrinsic three-dimensionality of the flow, Tomographic PIV (Tomo-PIV) was used to measure the velocity fields within the volume of fluid. Tomo-PIV measurements were made when the blade is rotating upwards to the horizontal position. The experimental setup is shown in Figure 1. A 8mm-thick laser light volume illuminated the flow at the suction side of the blade at the spanwise location of $0.25R$, where the turbulent separated flow was found to exist. The time separation between the pair of images was $\Delta t = 150\mu s$. The inline configuration was chosen in which the four cameras were mounted on the same side of the laser light volume, since the other side of the light was blocked by the nacelle. The angle between the principle axes of the cameras and the z direction ranged from about $5°$ to $45°$. The Tomo-PIV setup for the static airfoil was similar to Figure 1, in which the airfoil spans the entire width of the tunnel's test section. As in Lee & Wu [10] and Tang et al.[25], three-dimensional light intensity fields were firstly obtained using 7 iterations of FastMART algorithm in the software LaVision Davis 8.1.1. Volume self-calibration imbedded in the software was also applied to reduce the calibration errors. Recursive volumetric cross-correlations were then performed on the particle intensity fields to yield the three-dimensional velocity fields within the whole measurement volume. The final interrogation spot is 96×96×96 voxels with 75% overlap, resulting in 106×92×11 vectors per instantaneous velocity field with a vector spacing of 0.76 mm. The precision measurement uncertainties of the current ensemble size of 500 have been estimated for the turbulence statistics presented hereafter at a 95% confidence level according to the procedures in Figliola & Beasley [26]. The maximum uncertainties within the field of view for the studied turbulence statistics are tabulated in table 1. While the current precision uncertainties of the Reynolds stresses are comparable to past studies using PIV[27–29], the relative uncertainty of the Reynolds shear stress $< uv >$ for the airfoil is more than twice larger than for the blade due to the strongly unsteady reversed flow over the airfoil at large angle of attack in the $x-y$ plane. The reasons of the much higher relative uncertainty of $< vw >$ than that of another Reynolds shear stress $< uv >$ include (1) the RMS error of the out-of-plane velocity component of w is approximately twice as large as that of the in-plane components of u and v[30]; and (2) the magnitude of $< uv >_{max}$ is about five times as large as that of $< vw >_{max}$. Finally, the relatively large uncertainty of the precision terms is due to the fact that P_{ij} embodies multiplication of mean velocity gradient and Reynolds stresses. Using the method of Wilson & Smith[31], the bias or systematic uncertainties were estimated to be about 2% of V_r for the mean velocities, and 4∼8% of V_r^2 for the Reynolds stresses.

3 Results and Discussion

3.1 Mean Fields

The mean velocity field relative to the rotating blade at the middle of the measurement volume is presented in figure 2(a) while the mean velocities over the static

Table 1 Maximum precision measurement uncertainties, ϵ, at a 95% confidence level.

Statistics	Blade	Airfoil
Mean streamwise velocity U	ϵ_U/V_r=1.8%	ϵ_U/V_∞=3.0%
Mean vertical velocity V	ϵ_V/V_r=2.7%	ϵ_V/V_∞=4.0%
Mean spanwise velocity W	ϵ_W/V_r=1.8%	—
Mean velocity magnitude q	ϵ_q/V_r=2.5%	ϵ_q/V_∞=2.5%
Mean streamwise vorticity ω_x	$\epsilon_{\omega_x}/\omega_{z_{max}}$=1.1%	—
Mean wall-normal vorticity ω_y	$\epsilon_{\omega_y}/\omega_{z_{max}}$=1.1%	—
Mean spanwise vorticity ω_z	$\epsilon_{\omega_z}/\omega_{z_{max}}$=2.1%	$\epsilon_{\omega_z}/\omega_{z_{max}}$=3.2%
Streamwise Reynolds normal stress $\langle u^2\rangle$	$\epsilon_{\langle u^2\rangle}/\langle u^2\rangle_{max}$=10.7%	$\epsilon_{\langle u^2\rangle}/\langle u^2\rangle_{max}$=12.0%
Wall-normal Reynolds normal stress $\langle v^2\rangle$	$\epsilon_{\langle v^2\rangle}/\langle v^2\rangle_{max}$=7.0%	$\epsilon_{\langle v^2\rangle}/\langle v^2\rangle_{max}$=3.2%
Spanwise Reynolds normal stress $\langle w^2\rangle$	$\epsilon_{\langle w^2\rangle}/\langle w^2\rangle_{max}$=1.2%	—
Reynolds shear stress $\langle uv\rangle$	$\epsilon_{\langle uv\rangle}/\langle uv\rangle_{max}$=7.0%	$\epsilon_{\langle uv\rangle}/\langle uv\rangle_{max}$=16.7%
Reynolds shear stress $\langle vw\rangle$	$\epsilon_{\langle vw\rangle}/\langle vw\rangle_{max}$=40.0%	—
Production Pij	$\epsilon_{P_{ij}}/P_{ij,max} = 40 \sim 50\%$	$\epsilon_{P_{ij}}/P_{ij,max} = 40 \sim 60\%$

airfoil at AOA of 30° are shown in Figure 2(b) for comparison. These mean fields as well as the following statistics were obtained through ensemble averaging. Note the different orientations of the blade and the airfoil in the figure, which is due to the rotational speed of the blade in the $+y$ direction rendering the velocity vector of the incoming flow relative to the blade different from the freestream velocity for the airfoil. Firstly for the static airfoil case, massive flow separation over the entire suction surface can be observed in figure 2(b) showing large recirculation bubbles. This flow field is consistent with the well-known flow physics associated with the stalled airfoil at large angles of attack. However, as seen in figure 2(a), the rotation annihilates the large recirculation bubbles and the strong reverse flows in the separated flows behind the blade's suction surface. Another distinct feature caused by the rotation of the blade is the appearance of the strong spanwise flow (shown as the contour in figure 2), or radial flow, from blade's root to its tip, which is similar to the streamwise rotating channel flow in which spanwise flow was also observed to be produced due to rotation [21, 22]. The spanwise flow behind the rotating blade at large AOA has been believed to be mainly produced by the centrifugal force, $\Omega^2\mathbf{R}$[4]. Since the rotational speed Ω varies little around our measurement instant, it is therefore reasonably believed to have similar spanwise flow characteristics between our oscillating blade and the rotational blade. The three-dimensionality and complexity of the separated flow on the rotating blade during stall delay can be further observed by the streamlines in the insets which illustrate the flows in three different cross-sectional planes ($x-z$ planes) along the blade's chord. The spanwise velocity is observed to be stronger near the blades but to decrease further away. One-dimensional profiles of the mean velocities over both the blade and the airfoil along the y direction at the spanwise center of the measurement flow volume at the streamwise location of x/c=1 and x/c=1.5, respectively, are also presented in figure 2 in order to provide some quantitative data for future model validations. These two locations were chosen since turbulence statistics illustrated below are relatively strong. For the same purpose, one-dimensional profiles of other statistics are also presented hereafter.

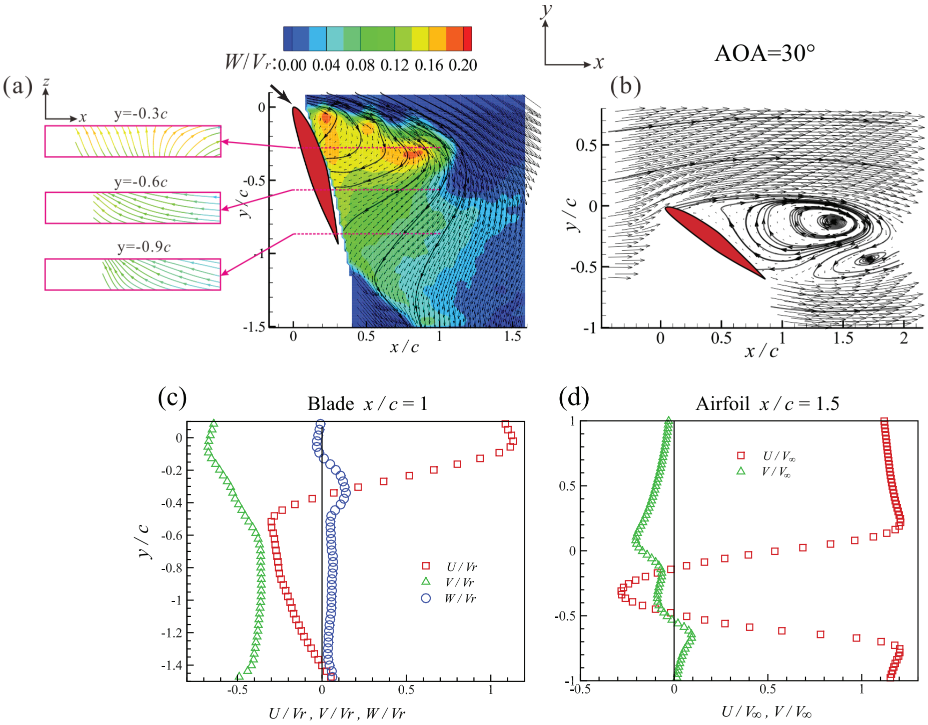

Fig. 2 (a) Mean velocity fields relative to the rotating blade. The vectors illustrate the velocity components U and V while the contour represents the velocity component W in the middle $x-y$ plane of the measurement fluid volume. Shown in the insets are the streamlines at three different cross-sectional planes ($x-z$ planes) along the blade's chord and the streamline colors indicate the magnitudes of W velocity component. The thick black arrow above the blade indicates the direction of the relative velocity V_r; (b) Mean velocity fields over the static airfoil; (c) One-dimensional profiles of mean velocities, U/V_r, V/V_r and W/V_r, over the blade along y direction at the spanwise center of the measurement volume and at x/c=1; (d) One-dimensional profiles of mean velocities, U/V_∞, V/V_∞, over the airfoil along y direction at the spanwise center of the measurement volume and at x/c=1.5.

The rotational effects on the shear layers can be observed from Figure 3 which shows the mean velocity magnitudes of the flows, $q=\sqrt{U^2+V^2+W^2}$, over both the rotating blade and the static airfoil. A readily observable feature is that the shear layers produced from both leading and trailing edges of the blade are slightly thicker, with less velocity gradient, than those of the airfoil. The waviness of the shear layer from the blade's leading edge is due to the persistence of the vortical structures [10]. In addition, the external flows immediately outside of the shear layers are obviously different between the cases of the blade and the airfoil, substantiating the speculation of Wood [3] that the external flow may be modified by the rotation during stall delay. Further, while the region of flow separation between the two shear layers for the airfoil case shrinks noticeably downstream, that of the blade does not appear so. In addition, the magnitudes of the velocities within the separated flow region recover much faster, than the airfoil case, from low values close to the blade's surface to substantial values further away from it.

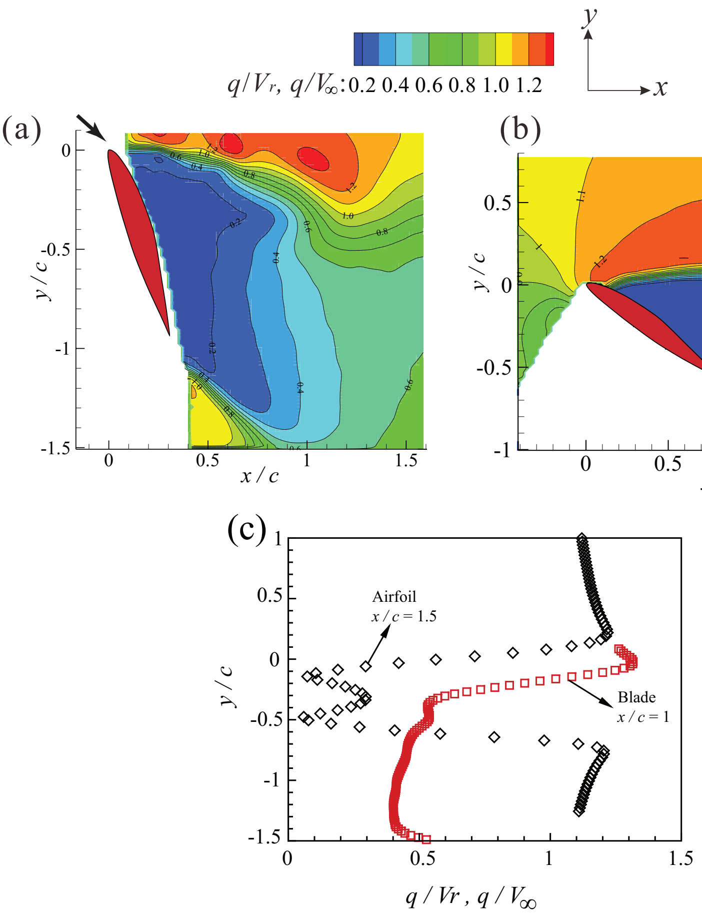

Fig. 3 Mean velocity magnitudes of the flows, $q = \sqrt{U^2 + V^2 + W^2}$, over (a) the rotating blade. The thick black arrow above the blade indicates the direction of the relative velocity V_r; (b) the static airfoil. (c) One-dimensional profiles of q over both blade and airfoil at the spanwise center of the measurement volume along y direction.

The mean vorticity fields for the blade and the airfoil are presented in Figure 4. While the two-dimensional mean flow over the static airfoil has only one mean vorticity component in the spanwise direction, the rotation of the blade produces extra mean vorticity components both in the streamwise and wall-normal directions, as seen in Figure 4(a) and (b). However, the magnitudes of ω_x and ω_y are much smaller than that of ω_z, which means that the vorticity vector in the flow over the blade is still mainly in the z direction, but slightly tilted in both x and y directions. Due to the large velocity gradients, the mean vorticity is concentrated at the shear layers generated from both leading and trailing edges of the blade and the airfoil. Interestingly, Figure 4(a) shows that the streamwise components of the mean vorticity are mainly negative at both shear layers. This is because the blade's rotational vector is in the $-x$ direction, too, and the rotation of the blade thus tilts the vorticity vector to the rotational direction. Since

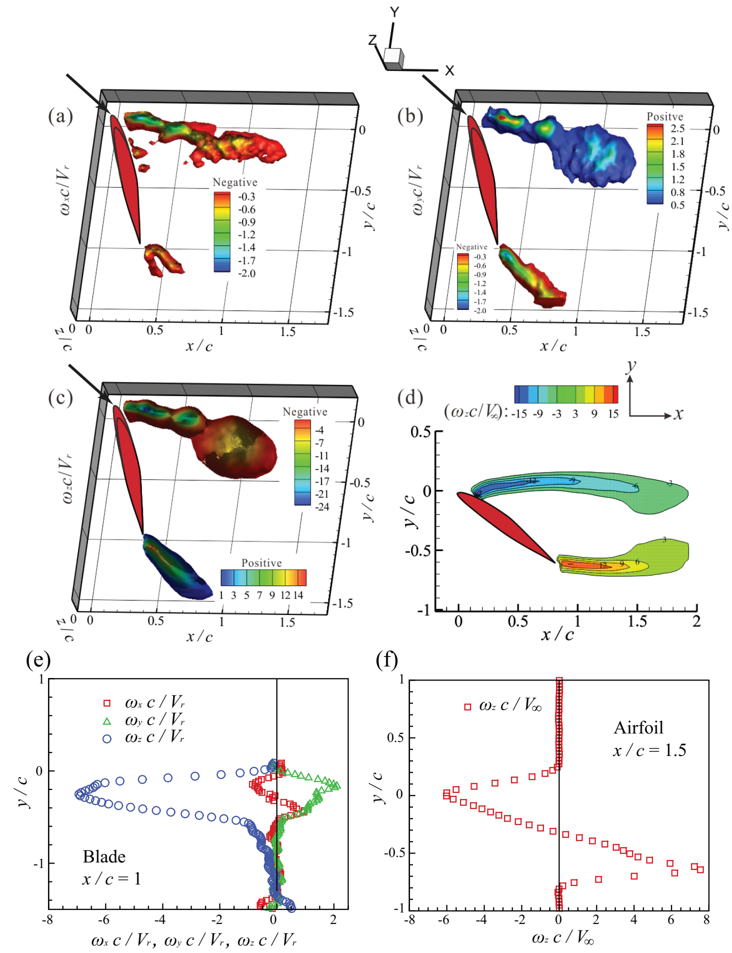

Fig. 4 (a) Mean streamwise vorticity, ω_x, over the blade; (b) Mean wall-normal vorticity, ω_y, over the blade; (c) Mean spanwise vorticity, ω_z, over the blade; The thick black arrow above the blade indicates the direction of the relative velocity V_r. (d) Mean spanwise vorticity, ω_z, over the airfoil. (e) One-dimensional profiles of ω_x, ω_y, and ω_z over the blade along y direction at the spanwise center of the measurement volume and at $x/c = 1$; (f) One-dimensional profile of ω_z over the airfoil along y direction at the spanwise center of the measurement volume and at $x/c = 1.5$.

$\omega_x = \partial W/\partial y - \partial V/\partial z$, the relatively large values of ω_x at the upper shear layer from the leading edge is mainly due to the $\partial W/\partial y$. Since the mean spanwise velocity component W is mostly created within the separated flow region by the rotation, from the freestream downward along the $-y$ direction into the separated flow, positive W velocity is obtained, thus producing strong negative values of $\partial W/\partial y$. However, at the lower shear layer from the trailing edge, the $\partial W/\partial y$ term is positive, but small since the W component close to the trailing edge of the blade is much smaller than in the upper shear layer. In any case, this positive $\partial W/\partial y$ term is slightly overweighed by the positive $\partial V/\partial z$ term to yield extremely small negative values of streamwise vorticity there. For the wall-normal vorticity component at the two shear layers, the major contribution is from the term involving the spanwise velocity, $\partial W/\partial x$. Given the fact that both shear layers are inclined in the $-y$ direction, $\partial W/\partial x$ is positive in the upper shear layer but negative in the lower one, resulting in the corresponding signs of ω_y. The effect of rotation on the major vorticity component ω_z is also significant, as seen in Figure 4(c) and (d). The drastically different distributions of U and V between the flows over the blade and the airfoil cause the remarkably distinct pattern of ω_z. There exist a few discrete peaks of ω_z along the upper shear layer of the blade, corresponding to the discrete coherent vortices observed there by Lee and Wu [10]. The streamwise sizes of ω_z at both layers are also clearly reduced by rotation.

3.2 Fluctuating Velocity Fields

Examples of instantaneous fluctuating velocity fields over the blade and the airfoil are presented in Figure 5. These fields are chosen because they are the significant contributors to the turbulent kinetic energy [32]. The velocity vector scales are the same between these two fields presented in this figure. A common feature is that the fluctuating velocities become stronger further downstream of the blade or airfoil. Not far from the airfoil's suction surface is the laminar-like flow due to extremely small fluctuating velocities, which is similar to the laminar-like flow in the recirculation region of the backward-facing-step flows [33, 34]. However, due to the rotation of the blade, the fluctuating velocities near the blade's suction surface are becoming much larger. Along the blade's leading-edge shear layer, two counter-rotating vortex pairs, which are circled in the figure, can be observed at about $x = 0.5c$ and $x = 1c$. Very strong v velocity components are induced in between the vortex pair located at $x = 1c$. In contrast, such vortex pairs do not appear along the airfoil's leading-edge shear layer. Further, while a few small counter-clock rotating vortices can be seen along the blade's trailing-edge shear layer, the fluctuating velocities at similar locations of the airfoil are too weak to observe any discernable vortices. The spanwise fluctuating flows over the blade and the airfoil are illustrated in the insets of the figures. Although the mean separated flow above the airfoil's suction surface is two-dimensional, the fluctuating field presents three-dimensionality with spanwise velocity components and velocity variation in the z direction. However, the spanwise velocity component in the fluctuating field over the arifoil is found to be weaker than that over the blade.

3.3 Reynolds Stresses

The normalized Reynolds normal stresses over both the blade and the airfoil are presented in Figure 6. The relative velocity, V_r and the freestream velocity V_∞ are used for normalizing the blade and airfoil flows, respectively. Since the turbulence statistics of the flow over the airfoil are two-dimensional, they are presented as planar contours rather than the three-dimensional contour surfaces as for the blade.

The three diagonal components of the Reynolds stress tensor, $\langle u^2 \rangle$, $\langle v^2 \rangle$, and $\langle w^2 \rangle$, have been found to be significantly changed by the blade's rotation, reflecting the drastic modification of the fluctuating velocity fields shown in Figure 5. For

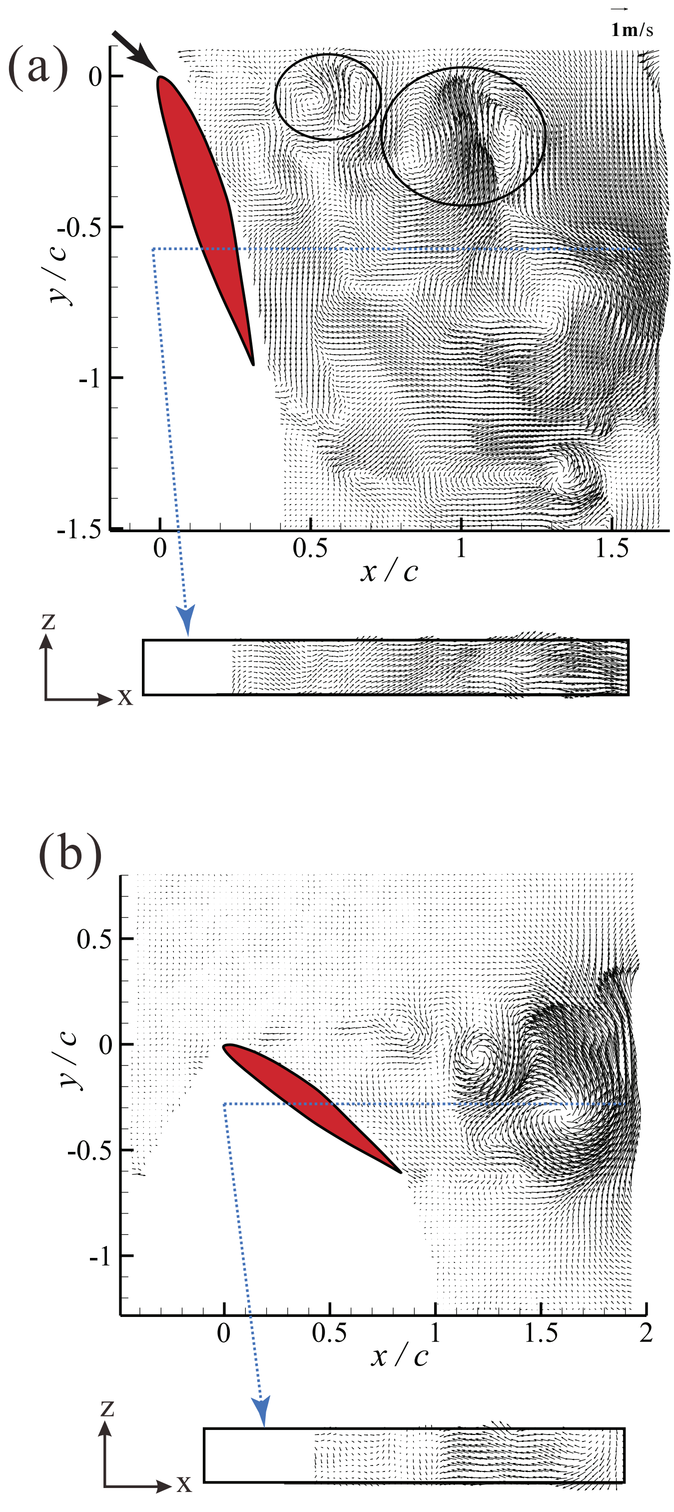

Fig. 5 Examples of instantaneous fluctuating velocity fields (a) over the blade and (b) over the airfoil. The insets present the velocity vectors in the cross-sectional plane ($x-z$ plane) at the location indicated by the dashed line to illustrate the instantaneous spanwise flow. The thick black arrow above the blade indicates the direction of the relative velocity V_r.

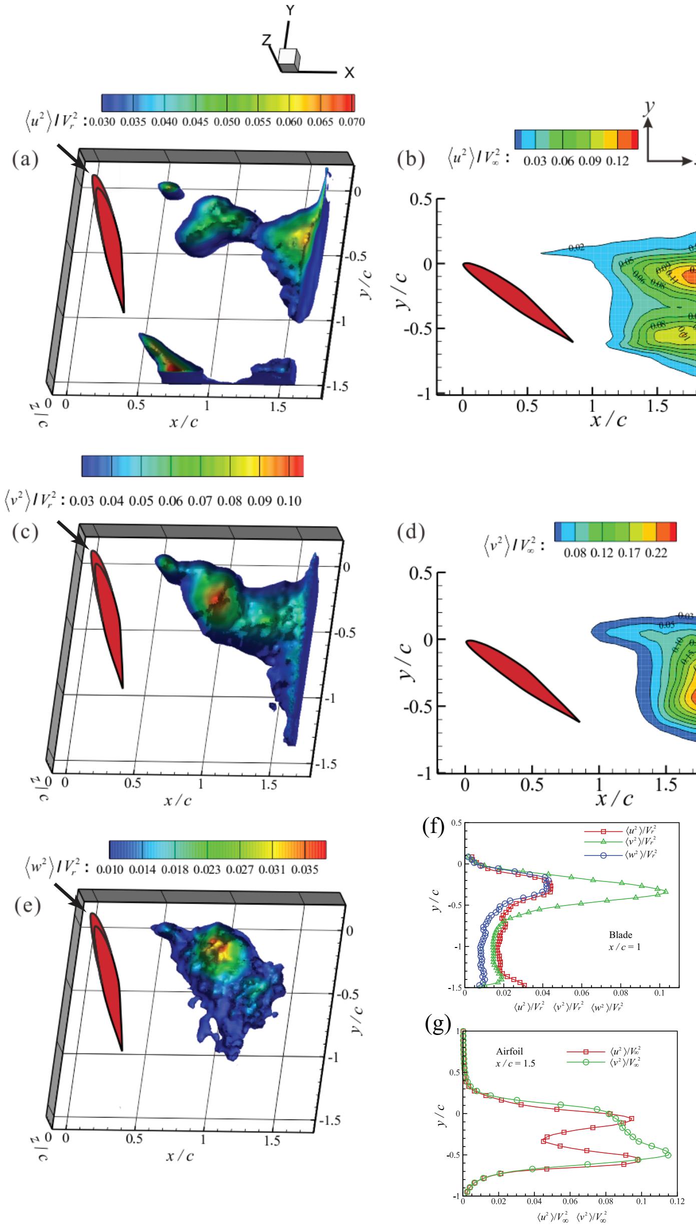

Fig. 6 Reynolds normal stresses. (a) Streamwise Reynolds normal stresss, $\langle u^2 \rangle$, over the blade; (b) $\langle u^2 \rangle$ over the airfoil; (c) wall-normal Reynolds normal stress, $\langle v^2 \rangle$, over the blade; (d) $\langle v^2 \rangle$ over the airfoil; and (e) spanwise Reynolds normal stress, $\langle w^2 \rangle$, over the blade. The thick black arrow above the blade indicates the direction of the relative velocity V_r. (f) One-dimensional profiles of Reynolds normal stresses over the blade along y direction at the spanwise center of the measurement volume and at x/c=1; (g) One-dimensional profiles of Reynolds normal stresses over the airfoil along y direction at the spanwise center of the measurement volume and at x/c=1.5.

the airfoil case, Figure 6(b) illustrates that negligible $\langle u^2 \rangle$ exists within one chord length from the leading edge above the airfoil's suction surface, while much higher values of $\langle u^2 \rangle$ are observed further downstream concentrating in two parallel regions aligned horizontally. Referring back to Figure 5, it can be understood that these two regions of high streamwise Reynolds normal stresses correspond to the large magnitudes of the fluctuating u velocity components induced by one large vortex generated there. While $\langle u^2 \rangle$ are negligible along the leading- and trailing-edge shear layers of the airfoil flow, Figure 6(a) shows that $\langle u^2 \rangle$ for the blade flow are concentrated there. In addition, along the leading-edge shear layer, $\langle u^2 \rangle$ are focused in three discrete regions in the current field of view. The first two regions closer to the blade's leading edge coincide with the two counter-rotating vortex pairs in Figure 5(a) while the third region corresponds to the large-scale flows there.

Figure 6(d) shows that appreciable values of $\langle v^2 \rangle$ are only obtained at least one chord length downstream from the leading edge of the airfoil, similar to $\langle u^2 \rangle$. The peak value of $\langle v^2 \rangle$ is noticeably higher than that of $\langle u^2 \rangle$. This region of high $\langle v^2 \rangle$ can be associated with the induced strong vertical flow on the right side of the large vortex seen in Figure 5(b). However, due to the existence of other flow structures on the left side of the large-scale vortex, the induced vertical velocities there are much weaker, rendering much smaller values of $\langle v^2 \rangle$ between $x = 1c$ and $x = 1.5c$. For the blade, $\langle v^2 \rangle$ are concentrated on the leading-edge shear layer, while having negligible values along the trailing-edge shear layer. The strongest $\langle v^2 \rangle$ in the present field of view occurs around the induced vertical flow in between the second vortex pair in Figure 5(a). The distribution of $\langle v^2 \rangle$ along the blade's leading-edge shear layer is similar to that of $\langle u^2 \rangle$, indicating that they may be associated with similar fluctuating flow structures such as the counter-rotating vortices in Figure 5(a).

The spanwise Reynolds normal stress, $\langle w^2 \rangle$, for the blade is about a magnitude smaller than the other two diagonal components, but still much larger than that for the airfoil flow due to the blade's rotation. The spatial distribution of $\langle w^2 \rangle$ for the blade flow is quite similar to that of $\langle v^2 \rangle$ and $\langle u^2 \rangle$ along the leading-edge shear layer, indicating that the same flow structures, as indicated above, are responsible for producing these three Reynolds normal stresses. $\langle w^2 \rangle$ measured for the airfoil flow are negligibly small, partly because the resolution of the current Tomo-PIV is too coarse to resolve them, and are therefore not presented here.

The normalized Reynolds shear stresses are presented in Figure 7. Since the Reynolds shear stresses with the spanwise velocity component are zero for the two-dimensional airfoil flow, they are therefore not shown. In addition, it was observed in this study that $\langle uw \rangle$ were extremely small, too, for the flow over the blade, and thus its plot is not included in Figure 7 either. The distributions of $\langle uv \rangle$ for both blade and airfoil are quite similar to those of $\langle u^2 \rangle$. $\langle uv \rangle$ along the blade's leading- and trailing-edge shear layers are mainly negative, indicating Q2 ($u < 0$ and $v > 0$) and/or Q4 ($u > 0$ and $v < 0$) vectors are dominant over Q1 ($u > 0$ and $v > 0$) and/or Q3 ($u < 0$ and $v < 0$) vectors there. Again, $\langle uv \rangle$ are stronger further away along the blade's leading-edge shear layer due to the increased fluctuating velocities. Although the wall-normal normal stress $\langle v^2 \rangle$ is larger at $x = 1c$ than further downstream, the velocities may be dominantly vertical with much smaller streamwise velocity component, as indicated in the induced flow in between the second vortex pair shown in Figure 5(a), and therefore

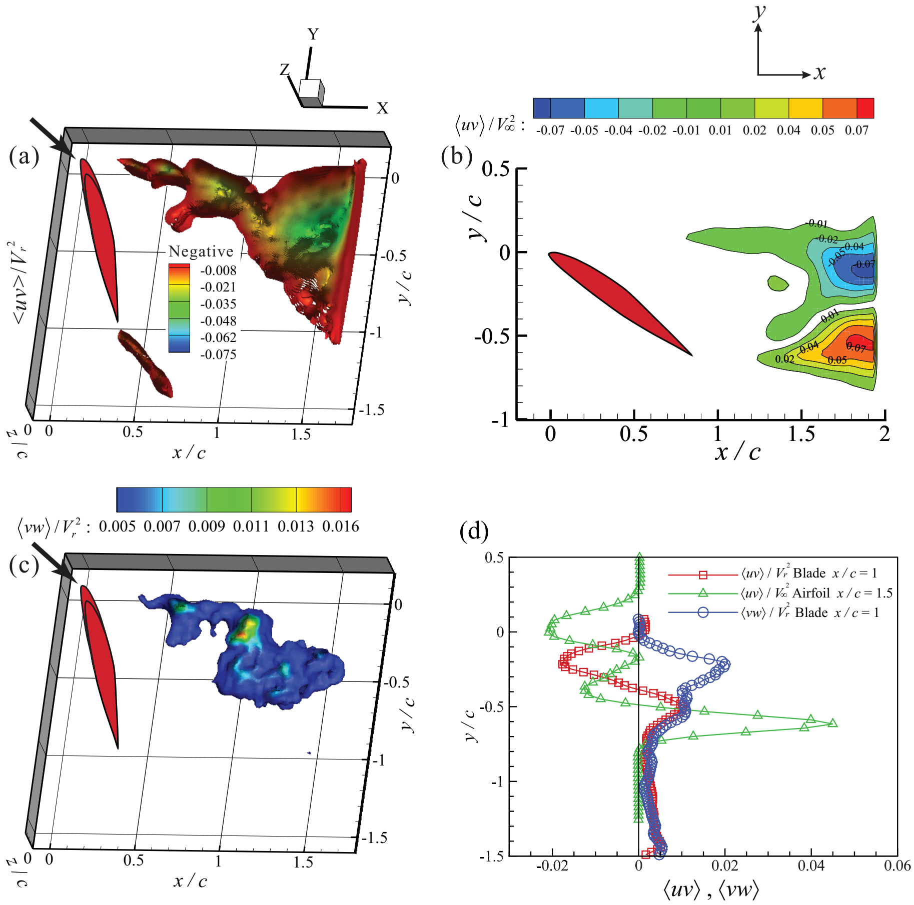

Fig. 7 Reynolds shear stresses. (a) Reynolds shear stress $\langle uv \rangle$ over the blade; (b) $\langle uv \rangle$ over the airfoil; and (c) $\langle vw \rangle$ over the blade. The thick black arrow above the blade indicates the direction of the relative velocity V_r. (d) One-dimensional profiles of Reynolds shear stresses over both blade and airfoil along y direction at the spanwise center of the measurement volume.

produce less shear stress $\langle uv \rangle$. The peak values of $\langle uv \rangle$ for the airfoil flow roughly coincide with those of $\langle u^2 \rangle$, indicating the major contribution from the strong streamwise velocity components at those locations. The opposite signs of $\langle uv \rangle$ for the airfoil case correspond to the opposite flow directions below and above a large-scale vortex there, as indicated in Figure 5(b). Most $\langle vw \rangle$ shear stresses are produced within $x = 1.5c$ along the blade's leading-edge shear layer. The positive values of $\langle vw \rangle$ indicate the positive correlation between strong wall-normal and spanwise fluctuating velocity components. The weak $\langle vw \rangle$ shear stress beyond $x = 1.5c$ is due to the much weaker w component further away from the blade's suction surface.

3.4 Turbulence Production Terms

The transport equation for the Reynolds stresses in a rotating frame of reference for an incompressible fluid is written as [35]

$$\frac{\partial\langle u_i u_j\rangle}{\partial t}+U_k\frac{\partial\langle u_i u_j\rangle}{\partial x_k}=-\left(\langle u_i u_k\rangle\frac{\partial U_j}{\partial x_k}+\langle u_j u_k\rangle\frac{\partial U_i}{\partial x_k}\right)-2\Omega_m\left(\epsilon_{mki}\langle u_j u_k\rangle+\epsilon_{mkj}\langle u_i u_k\rangle\right)$$
$$+\nu\frac{\partial^2\langle u_i u_j\rangle}{\partial x_k\partial x_k}-\frac{\varepsilon}{k}\langle u_i u_j\rangle+\wp_{ij}-\frac{\partial\Pi_{ijk}}{\partial x_k}, \quad (2)$$

where ϵ_{ijk} is the permutation tensor, Ω_i is the i^{th} component of the angular velocity vector of the reference frame, and ε is the dissipation. The first term on this equation's right-hand side is the production tensor due to the mean velocity gradient (P_{ij}) and the second term is the production due to the frame rotation (G_{ij}). Since the present frame rotation vector is $\vec{\mathbf{\Omega}}=-\Omega_x\ \vec{\mathbf{i}}$, the components of G_{ij} are

$$\begin{gathered}G_{11}=0, G_{22}=-4\Omega_x\langle vw\rangle, G_{33}=4\Omega_x\langle vw\rangle,\\ G_{12}=-2\Omega_x\langle uw\rangle, G_{13}=2\Omega_x\langle uv\rangle, G_{23}=2\Omega_x(\langle v^2\rangle-\langle w^2\rangle).\end{gathered} \quad (3)$$

The fifth term on the right side of equation 2 is given by

$$\wp_{ij}=-\langle\frac{p}{\rho}\left(\frac{\partial u_i}{\partial x_j}+\frac{\partial u_j}{\partial x_i}\right)\rangle-\varepsilon_{ij}+\frac{\varepsilon}{k}\langle u_i u_j\rangle, \quad (4)$$

which is a traceless redistribution tensor. ε_{ij} is the rate of viscous dissipation which is given by $\varepsilon_{ij}=\nu\langle\frac{\partial u_i}{\partial x_k}\frac{\partial u_j}{\partial x_k}\rangle$. Π_{ijk} in the sixth term of equation 2 is

$$\Pi_{ijk}=\langle u_i u_j u_k\rangle+\frac{\delta_{ki}}{\rho}\langle u_j p\rangle+\frac{\delta_{kj}}{\rho}\langle u_i p\rangle, \quad (5)$$

which represents the turbulent and pressure diffusion. In shear layers that obey the thin shear layer approximation, the production terms of the turbulent kinetic energy dominate while other terms receive their energy largely through the pressure-velocity terms. Therefore, the rotational effects on these production terms are examined in this section.

Since $G_{11}=0$, blade's rotation does not directly affects the production of $\langle u^2\rangle$, which, however, is indirectly affected by rotation through the modification of the fluctuating velocity fields and thus the Reynolds stresses and mean velocity gradients. Due to the two-dimensional flow for the airfoil case, and negligible $\langle uw\rangle$ and spanwise variation of U for the blade's flow, P_{uu} for both cases are essentially the summation of mean strain production term $-2\langle u^2\rangle\partial U/\partial x$ and mean shear production term $-2\langle uv\rangle\partial U/\partial y$. Figure 8(a) shows that, for the blade flow, P_{uu} are mostly positive and concentrated along the two shear layers with smaller parts of the regions with weaker negative values. Across the inclined leading-edge shear layer, $-2\langle u^2\rangle\partial U/\partial x$ tends to be negative while $-2\langle uv\rangle\partial U/\partial y$ is positive, the balance between these two terms created P_{uu} of different signs at different regions. At the leading-edge shear layer, it appears that the mean shear production term dominates. On the other hand, across the trailing-edge shear layer, the signs of the mean strain and shear production terms are opposite to those at the other shear

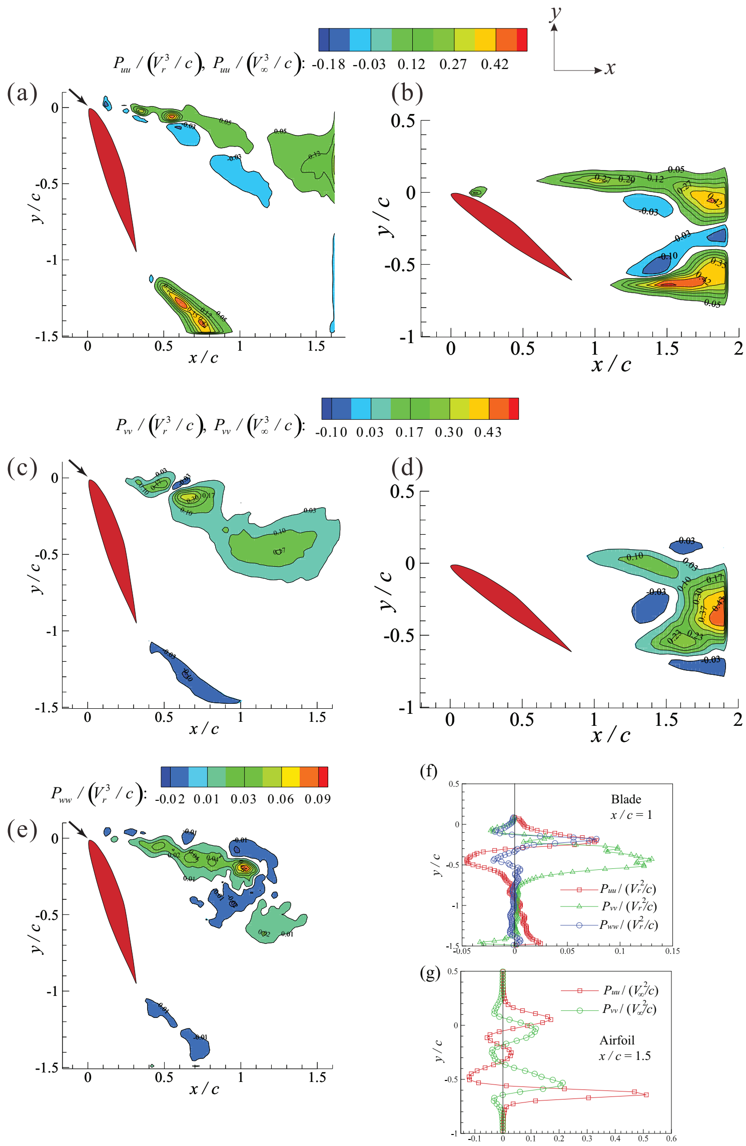

Fig. 8 Production terms, P_{uu}, P_{vv}, and P_{ww}. (a) P_{uu} over the blade; (b) P_{uu} over the airfoil; (c) P_{vv} over the blade; (d) P_{vv} over the airfoil; and (e) P_{ww} over the blade. The thick black arrow above the blade indicates the direction of the relative velocity V_r. (f) One-dimensional profiles of P_{uu}, P_{vv}, and P_{ww} over the blade along y direction. (g) One-dimensional profiles of P_{uu} and P_{vv} over the airfoil along y direction.

layer. Therefore, positive P_{uu} there indicate that the mean strain production term dominates at the trailing-edge shear layer. For the airfoil, Figure 8(b) shows that P_{uu} are focused far downstream as the distribution of $\langle u^2 \rangle$. Due to the flip of the sign of $\langle uv \rangle$ across both shear layers of the airfoil flow, both mean strain and mean shear production terms are positive. Inside the shear layers of the airfoil flow, some quite strong negative P_{uu} can be observed, which are therefore the sinks of $\langle u^2 \rangle$ at those parts of the separated flow over the airfoil.

Similarly, P_{vv} is mainly balanced by the two terms $-2\langle uv \rangle \partial V/\partial x$ and $-2\langle v^2 \rangle \partial V/\partial y$ for both flows over the blade and the airfoil. While P_{vv} are mostly positive along the blade's leading-edge shear layer, they are negative along the trailing-edge layer. The distribution of P_{vv} for the airfoil flow is quite similar to $\langle v^2 \rangle$ indicating a dominant mean strain production term. Blade's rotation does have a direct influence on the production of wall-normal Reynolds normal stress through the G_{22} term (see equation 3). The distribution of $\langle vw \rangle$ shown in Figure 7(c) indicates that the blade's rotation generated sinks for $\langle v^2 \rangle$ mostly within $x = 1.5c$ along the leading-edge shear layer while the direct rotational effects on the production of $\langle v^2 \rangle$, G_{22}, at other parts of the flow are quite small.

While $P_{ww} = 0$ for the two-dimensional airfoil flow, it is mainly contributed by the term $-2\langle vw \rangle \partial W/\partial y$ for the blade flow. Since $\langle vw \rangle$ is positive, P_{ww} is therefore mostly positive along the leading-edge shear layer while negative along the trailing-edge layer due to the different signs of $\partial W/\partial y$, as illustrated in Figure 8(e). In addition, the rotation contributes sources of the production $\langle w^2 \rangle$ through the positive values of G_{33}.

Because $G_{ii} = 0$, the blade's rotation therefore does not directly affect the production of the turbulent kinetic energy, $P = \frac{1}{2} P_{ii}$, which is however indirectly affected through the drastically modified velocity fields. In addition, the rotation redistribute the kinetic energy among the components, through the G_{22} and G_{33} terms, by extracting the energy from $\langle v^2 \rangle$ to transfer to $\langle w^2 \rangle$.

Figure 9(a) shows that P_{uv} are all negative along both shear layers of the blade's flow while P_{uv} along the leading-edge layer is much stronger. Since $\langle uv \rangle$ in the leading- and trailing-edge shear layers are negative, P_{uv} therefore increases the magnitudes of the Reynolds shear stress $\langle uv \rangle$ there. The rotational production term $G_{12} = -2\Omega_x \langle uw \rangle$ contributes very little to the production of $\langle uv \rangle$ of the blade flow due to the negligible values of $\langle uw \rangle$. The distribution of P_{uv} of the airfoil flow, as illustrated in Figure 9(b), is quire similar to that of $\langle uv \rangle$ and therefore P_{uv} provides sources to this Reynolds shear stress. As seen in Figure 9(c), P_{vw} for the blade flow is mostly positive along the leading-edge shear layer, which thus increases the value of positive Reynolds shear stress $\langle vw \rangle$ there. Blade's rotation provides sources to $\langle vw \rangle$, too, since $G_{23} = 2\Omega_x(\langle v^2 \rangle - \langle w^2 \rangle)$ is positive along the leading-edge layer. Finally, although the Reynolds shear stress $\langle uw \rangle$ is very small, the production term P_{uw} has negative values whose magnitudes are comparable to that of P_{vw} along the leading-edge shear layer. In addition, the rotational production term $G_{13} = 2\Omega_x \langle uv \rangle$ is observed to achieve quite significant negative values. However, these large amount of productions of $\langle uw \rangle$ along the blade's shear layers are eventually diffused, dissipated, and redistributed by other terms in the Reynolds stress transport equation.

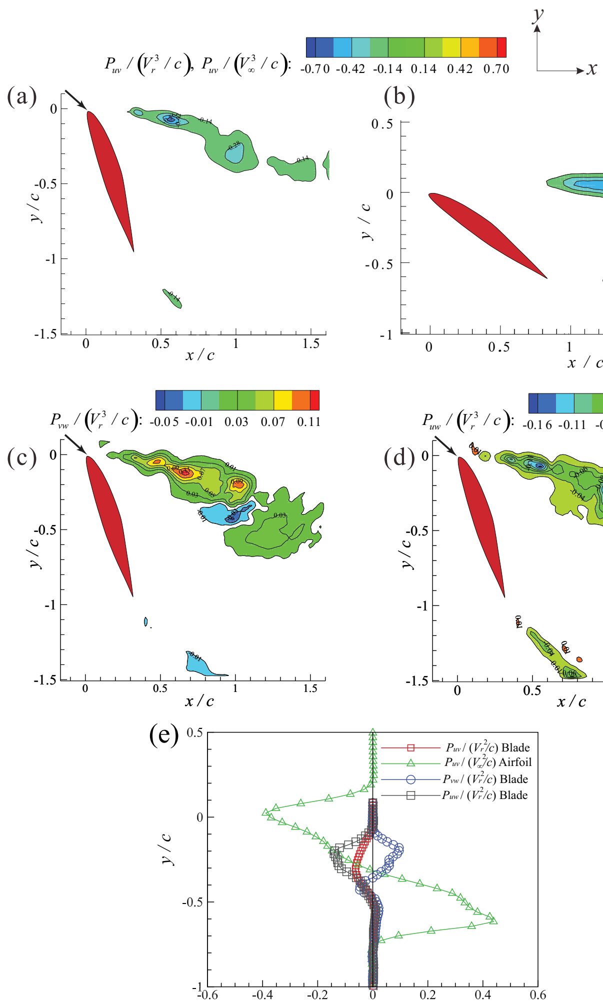

Fig. 9 Production terms P_{uv}, P_{uw}, and P_{vw}. (a) P_{uv} over the blade; (b) P_{uv} over the airfoil; (c) P_{uw} over the blade; and (d) P_{vw} over the blade. The thick black arrow above the blade indicates the direction of the relative velocity V_r. (e) One-dimensional profiles of P_{uv}, P_{uw}, and P_{vw} over the blade and airfoil along y direction.

3.5 Enstrophy

The distributions of the enstrophy $\langle \omega_i' \omega_i' \rangle$, where ω_i' is the i^{th} component of the fluctuating vorticity, for both blade and airfoil flows are presented in Figure 10. Similar to other turbulence statistics, enstrophy of the blade flow is mainly confined closer to the blade's leading and trailing edges along the two shear layers while that of the airfoil flow are focused further downstream from the airfoil's edges. While the magnitudes of enstrophy along the leading- and trailing-edge shear layers of the airfoil flow are quite similar, those at the leading-edge layer of the blade flow are much higher than at the trailing-edge layer. It is known [18] that

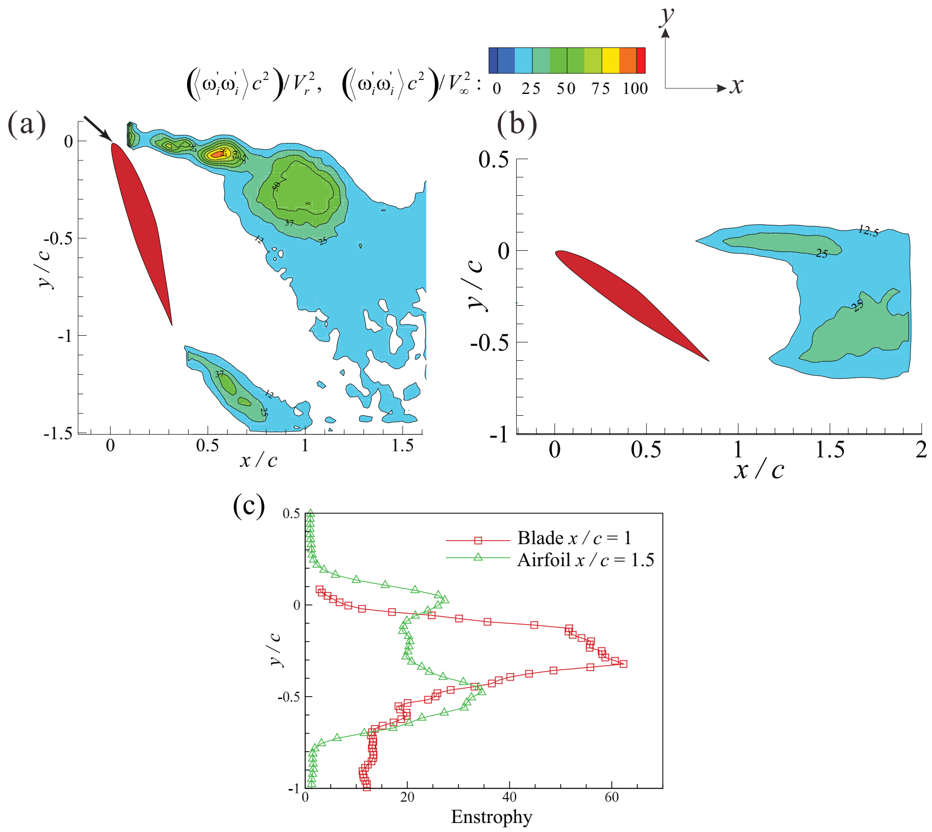

Fig. 10 Distributions of enstrophy, $\langle\omega_i'\omega_i'\rangle$, (a) over the blade and (b) over the airfoil. The thick black arrow above the blade indicates the direction of the relative velocity V_r. (c) One-dimensional profiles of enstrophy over the blade and airfoil along y direction.

fluctuating vorticity is primarily associated with the small-scale turbulence and therefore the distribution of enstrophy roughly resembles that of the turbulence energy dissipation. As such, Figure 10 indicates that the turbulent kinetic energies of the blade flow are mainly dissipated along the shear layers, too, particularly along the leading-edge layer.

4 Summary and Conclusions

Three-dimensional velocity fields were measured using Tomo-PIV on a model of the wind turbine blade to study the effects of rotation on the separated turbulent flow during stall delay of the blade. The measurements were conducted at Re≈4800 and a global TSR of 3 which is much lower than the design TSR of 6. For comparison, the flow fields on a static airfoil were also measured at similar AOAs and Re using Tomo-PIV. The following significant changes have been observed in both the mean flow fields and the turbulence statistics made by the blade's streamwise rotation:

1. The most obvious difference between the mean flow field for the blade and that for the static airfoil is that the massive recirculation which forms above the surface of the static airfoil does not exist.
2. The blade's rotation created a spanwise or radial flow from blade's root to tip within the separated flow region.
3. While the major mean vorticity component of the blade's flow was still in the spanwise (z) direction, the rotation of the blade generated extra mean vorticity components in the other two directions, making the mean vorticity vector slightly tilted, not only towards the blade's rotational direction but also towards the wall-normal direction.
4. Due to the drastically different distributions of the mean velocity fields in the separated flow region, the distributions of the major mean vorticity component, ω_z, were also found to be distinct between the blade and the airfoil cases.
5. While the turbulence statistics were concentrated along the leading-edge shear layer of the blade flow, they were mainly located quite far downstream of the airfoil's suction surface.
6. Some of the Reynolds stress components involving the spanwise fluctuating velocity were observed to be particularly affected by the blade's rotation which enhanced the spanwise Reynolds normal stress $\langle w^2 \rangle$ and created noticeably high values of shear stress $\langle vw \rangle$.
7. The production of the Reynolds stresses were affected by the rotation both directly through the rotation production terms and indirectly by changing the fluctuating velocity fields. The rotation production terms were found to provide sources to $\langle w^2 \rangle$ but sinks to $\langle v^2 \rangle$. As such, the direct effect of blade's rotation on the turbulent kinetic energy is to extract energy from $\langle v^2 \rangle$ to transfer to $\langle w^2 \rangle$. In addition, the direct effects of rotation included providing sources to $\langle vw \rangle$ and sinks to $\langle uw \rangle$.

Acknowledgements This project is supported by the Ministry of Education in Singapore under the projects ARC 22/12, RG52/11, and RG90/13.

References

1. D. Wood, Journal of Wind Engineering and Industrial Aerodynamics **37**, 1 (1991)
2. H. Dumitrescu, V. Cardos, AIAA Journal **42**, 408 (2004)
3. D. Wood, AIAA Journal **43**, 2268 (2005)
4. D. Hu, O. Hua, Z. Du, Renewable Energy **31**, 821 (2006)
5. S.P. Breton, F.N. Coton, G. Moe, Wind Energy **11**, 459 (2008)
6. H. Dumitrescu, V. Cardos, Journal of Applied Mathematics and Mechanics **89**, 163 (2009)
7. H. Dumitrescu, F. Frunzulica, V. Cardos, Journal of Aircraft **50**, 315 (2013)
8. R. Yang, R.N. Li, W. Han, D.S. Li, Modern Physics Letters B **23**, 505 (2009)
9. H. Lee, Y. Wu, Chinese Physics Letters **30**(6), 064703 (4 pp.) (2013)
10. H. Lee, Y. Wu, Journal of Wind Engineering and Industrial Aerodynamics **123**, 56 (2013)
11. H. Lee, Y. Wu, Wind Energy **18**(7), 1185 (2014)
12. J. Johnston, International Journal of Rotating Machinery **4**, 97 (1998)
13. G. Brethouwer, Journal of Fluid Mechanics **542**, 305 (2005)
14. R. Kristoffersen, H. Andersson, Journal of Fluid Mechanics **256**, 163 (1993)
15. J. Pallares, L. Davidson, Physics of Fluids **12**, 2878 (2000)
16. J. Johnston, R. Halleen, D. Lezius, Journal of Fluid Mechanics **56**, 533 (1972)
17. S. Julien, G. Dumas, F. Torriano, Y. Maciel, International Journal of Computational Fluid Dynamics **22**(1-2), 19 (2008)
18. M. Barri, H.I. Andersson, Journal of Fluid Mechanics **665**, 382 (2010)

19. J. Visscher, H.I. Andersson, Physics of Fluids **23**, 075108 (2011)
20. H. Wu, N. Kasagi, Physics of Fluids **16**(4), 979 (2004)
21. I. Recktenwald, T. Weller, W. Schroder, M. Oberlack, Physics of Fluids **19**(8), 085114 (2007)
22. N. Alkishriwi, M. Meinke, W. Schroder, Computers and Fluids **37**(7), 786 (2008)
23. T. Burton, N. Jenkins, D. Sharpe, E. Bossanyi, *Wind energy handbook*, 2nd edn. (John Wiley and Sons, 2012)
24. J.G. Manwell, J.G. McGowan, A.L. Rogers, *Wind Energy Explained: Theory, Design and Application* (Wiley InterScience, 2002)
25. H. Tang, P. Salunkhe, Y. Zheng, J. Du, Y. Wu, Experimental Thermal and Fluid Science **57**, 1 (2014)
26. R.S. Figliola, D.E. Beasley, *Theory and Design for Mechanical Measurements*, 5th edn. (John Wiley & Sons, Inc., 2011)
27. Y. Wu, K.T. Christensen, AIAA J. **44**, 3098 (2006)
28. H. Ren, Y. Wu, Phys. Fluids **23**, 045102 (2011)
29. H.R..Y. Wu, International Journal of Heat and Fluid Flow **40**(15-31) (2013)
30. G. Elsinga, F. Scarano, B. Wieneke, B. Oudheusden, Experiments in Fluids **41**, 933 (2006)
31. B. Wilson, B. Smith, Meas. Sci. Technol. **24**(035301), 11pp (2013)
32. Y. Wu, Physics of Fluids **26**, 045113 (2014)
33. H. Le, P. Moin, J. Kim, Journal of Fluid Mechanics **330**, 349 (1997)
34. Y. Wu, H. Ren, H. Tang, International Journal of Heat and Fluid Flow **44**, 155 (2013)
35. M. Oberlack, W. Cabot, B. Pettersson Reif, T. Weller, Journal of Fluid Mechanics **562**, 383 (2006)